

One-shot Measurement of Thermal *and* Kinematic Fields: InfraRed Image Correlation (IRIC)

A. Maynadier · M. Poncelet · K. Lavernhe-Taillard · S. Roux

Received: 2 July 2010 / Accepted: 28 February 2011 / Published online: 29 March 2011
© Society for Experimental Mechanics 2011

Abstract Joint kinematic and thermal full field measurement provides rich and relevant information on the thermomechanical properties of materials. A new experimental method is proposed to measure both these fields simultaneously. Although solely based on images captured with a unique infrared camera, it affords both kinematic and thermal fields. It consists of an enriched global Digital Image Correlation technique, where the variation of optical flow due to the local displacement and the change of temperature are jointly evaluated through a decomposition over a finite element mesh. After an *a priori* evaluation of the performance of the method on synthetic cases, a first experimental application to a Shape Memory Alloy specimen under tension is done. It is shown that the method is able to capture localized transformation bands which are a few pixel wide.

Keywords Digital image correlation · Quantitative infrared thermography · Thermo-mechanical full field measurements · Shape memory alloy

Introduction

Full field kinematic measurements have been more and more frequently used in the broad field of experimental mechanics, from micro [1] to macro scale [2]. Besides, global and spatially resolved thermal field measurements are more and more commonly and successfully used since the 90s because of the generalization of focal plane array cameras, aiming at quantitative InfraRed Thermography (IRT). In numerous applications, the measurement of both thermal and kinematic fields offers invaluable experimental data to be compared to or to assist numerical simulations (e.g. providing actual boundary conditions). Such comparisons are crucial for checking energy balance when local heat sources and mechanical work are sought, opening the way to *in situ* calorimetry experiments [3]. In this case, it is of the utmost importance to correct local displacements of the physical point [4] or to take into account the variation of conductivity with strain [5]. Finally, joint thermal and kinematic full fields will lead to unprecedented identifications of thermo-mechanical or thermo-dynamical models.

All these applications require a precise registration of the measurements at the exact same spatial and temporal coordinates. Unfortunately, thermal and kinematic techniques generally require different imaging devices with their own specific optics, spatial resolutions and acquisition rates. The space and time association of both fields during *a posteriori* data processing is thus a real difficulty, giving place to interpolations which degrade information enough to significantly distort high spatial and temporal gradient phenomena. From an experimental point of view, the two techniques

A. Maynadier (✉) · M. Poncelet · K. Lavernhe-Taillard (SEM member) · S. Roux
Laboratoire de Mécanique et Technologie (LMT-Cachan),
ENS de Cachan/CNRS UMR, 8535/Univ. Paris 6/PRES
UniverSud Paris, 61 Avenue du Président Wilson,
94235 Cachan Cedex, France
e-mail: anne.maynadier@lmt.ens-cachan.fr

M. Poncelet
CEA Saclay, DEN-DANS/DMN/SRMA/LC2M,
91191 Gif Sur Yvette Cedex, France

are also difficult to set up simultaneously as they call for different (or even contradictory) environments:

- Most of the time IRT requires a uniform coating on the area of interest to obtain an artificial high, homogeneous and constant emissivity. On the contrary, kinematic full field measurements (such as grid method or Digital Image Correlation (DIC)) need a heterogeneous and contrasted texture, with a grey level range as large as possible over short distances. A “usual” DIC speckle has a rather low emissivity (about 70%) in the middle wave infrared wavelength band, with a non-negligible heterogeneity of emissivity when accurate thermal measurements are to be done (about 5%).
- IR cameras record a combination of the sample own emission and reflections of the surrounding radiations. An insulation from the surrounding heat sources is thus needed for IR measurement. On the contrary, techniques like DIC require a uniform and intense lighting to enhance the grey level dynamic range and to minimize the exposure time and the aperture. The installation of incandescent spotlights is often chosen, in spite of their perturbation on the IR measurement.
- From a practical point of view, both imaging systems and their dedicated equipment (lighting, power supplies, computers and wires) clutter around the testing machine. Access to the specimen is therefore uneasy. The user’s motions around the set up are limited and adding extra measuring devices is very difficult, if not impossible.
- Last, but not least, this combination of elements is expensive.

Some clever methods aiming at joint measurements have nonetheless been elaborated by different research teams, proposing palliative elements to partly circumvent the aforementioned difficulties.

First, the assumption that the temperature and the displacements are constant throughout the thickness is verified if the latter is sufficiently thin. Thus, IRT and DIC measurements can be performed indifferently on either side of thin geometries (sheets, plates or wires), on which adequate coatings have been deposited to accurate measurements [3, 6]. Nevertheless, the problem of time and space associations still remains since two cameras are used.

Second, Orteu et al. [7] propose to measure fields of different natures with a doublet of high-resolution CCD cameras focused on the same face of an extended 3D sample. To measure both the shape, the displacement, and an apparent temperature, an area is covered by black and white speckle, another is left bare

and a speckle pattern is video-projected on it during the shape measurement by stereo-correlation. So, over these disjointed surfaces, it is possible to obtain, from a unique set of images, kinematics fields on the one hand and 3D shape measurement on the other hand. Moreover, such cameras also record radiations in the Near Infra Red (NIR) wavelength band, so that they deliver a temperature information provided the surface is around 400–700°C. Because the emissivity of the surface is neither uniform nor calibrated, the thermal fields cannot be interpreted as the surface temperature, but only as an apparent temperature (i.e., a radiation intensity). Consequently joint kinematic and thermal fields are not *stricto sensu* measured on the same area, only shape and radiation are.

Third, it is possible to use two imaging systems to measure both fields on the same surface, using a speckle for full-field displacement measurement, coarse enough for enabling accurate thermal measurement “in” the high emissivity dots of the speckle [8]. Even though the spatial resolution of the thermal field is lesser than the one of the kinematical one, and the fact that synchronisation and association has to be done, both fields cover the exact same area.

Last, one can acquire both fields with a similar spatial resolution, using two imaging systems over the same surface. The point is then to work out a coating which is as uniform and high as possible in IR emissivity while heterogeneous in the visible spectrum. A first example of such a technique at microscopic scale is proposed by [9]. They use a “smart coating” to focus on the same surface an IR camera and a visible one via a beam-splitter set-up. Unfortunately, heterogeneities of emissivity are revealed when the thermal equilibrium between sample and the surrounding is no longer verified, since high emissivity dots give information about surface temperature, while low emissivity dots provide a signal which is a combination of the sample and surrounding temperatures. However, even if a better coating is designed, the method requires two imaging systems so that image association and synchronization remain to be performed.

To avoid this double difficulty (association due to two different imaging systems and conflicting requirements for the coating) this article aims at introducing a new experimental method to obtain both kinematic and thermal fields on a same surface over the exact same space and time discretization, and this with a single IR camera. Since emissivity heterogeneities are unavoidable, rather than try to minimize them, it is chosen to exploit them. Indeed, our coating has deliberately been designed to present a speckle of emissivity. Thus, the recorded IR images are contrasted enough to perform

DIC analyses in order to obtain reliable displacement fields. Moreover, since the images are recorded in the IR spectrum, the perceived grey level of each material point evolves with both the specimen and the surrounding temperature. It would only depend on the sample temperature, if the emissivity were equal to 1 strictly, which is impossible to get in practice, even with black carbon powder. Nonetheless this evolution solely carries the information of the surface temperature we are looking for, provided that the surrounding radiative contribution is constant.

The key point of the proposed method is that the fundamental optical flow conservation assumption, usually necessary to DIC computation, is no longer valid since the perceived grey level also evolves with the temperature. Consequently, this assumption has to be modified to take into account the local temperature variation. A calibration is also needed to identify the parameters describing the variation of optical flow with the local sample temperature. The calibration parameters depend on the whole set-up, namely the coating, the ambient radiations, the atmosphere permittivity, the optical and acquisition adjustments. Finally, we are able to jointly determine, with a single imaging equipment, over a single surface, coupled thermal and kinematic fields.

The coating design and the measurement basis principle are presented in Section “[Measurement Basis Principle](#)”. The calibration performed in order to extract the temperature information from the speckle grey level variation is detailed in Section “[Prior Coating Calibration](#)”. Section “[Mathematical Formulation and Numerical Algorithm](#)” presents the mathematical formulation deduced from the previous observations and the way it has been implemented as an adaptation of a global finite-element based DIC algorithm. In this section, the extraction of the two types of information from the minimization of a single objective function is detailed. An uncertainty analysis will be carried out in Section “[Numerical Algorithm Uncertainty](#)”. The IRIC technique is then applied to a uniaxial tensile test on a Ni-Ti Shape Memory Alloy (SMA). Indeed, these alloys are well known for their pseudo-elasticity, due to a martensitic transformation localized in bands. Experimental results are presented and discussed in Section “[Application: Tensile Test on Ni-Ti SMA](#)”. A brief summary and some perspectives conclude this paper.

Measurement Basis Principle

We aim at obtaining both kinematic and thermal fields. The latter is generally obtained thanks to the record of

the IR emissions, known to be function of both temperature and emissivity of the surface as described below [equation (1)]. The camera conversion between radiation intensity and temperature is performed thanks to a regulated extended high emissivity black body. To have the most accurate measurement, the emissivity of the sample surface has to be as uniform as possible and is often artificially increased by covering the region of interest with high emissivity black paint or carbon black (typically $\epsilon > 0.96$). The intensity of perceived radiations, R_p of an opaque body, in each point, can be written as [10]

$$R_p = \epsilon_1 R_t + (1 - \epsilon_1)\Phi \quad (1)$$

where ϵ_1 is the emissivity of the observed surface and Φ the surrounding radiations being partly reflected over the observed surface. R_t , the spectral exitance is the power radiated per unit of area over all wavelengths for a surface temperature T_1 . The Stefan-Boltzmann law states that

$$R_t = \sigma_{SB} T_1^4 \quad (2)$$

where $\sigma_{SB} = 5.67 \times 10^{-8} \text{ Wm}^{-2}\text{K}^{-4}$.

The first term in equation (1) represents the specimen emission whereas the second one represents the surrounding radiations reflected on (or scattered from) the sample. Indeed, when the emissivity approaches unity, $\epsilon_1 \simeq 1$, the surrounding radiations can be neglected and R_p gives a reliable signal for measuring the sample temperature.

The correspondence between the camera Digital Level (DL) and the actual temperature in Celsius degrees is a non-linear function which captures both the non-linearity of the Stefan-Boltzmann law, equation (2), and the specific sensitivity of the camera. Consequently, such a temperature evaluation over a sample is in most (if not all) cases performed with the most homogeneous emissivity achievable.

In contrast, a speckle pattern with sharp contrasts is needed to perform a DIC analysis. In order for the latter to be captured by the IR camera, a speckle pattern of non-uniform emissivity is to be deposited on the sample surface. Henceforth, measuring displacement or temperatures calls for antagonist properties of the specimen surface. The present study proposes a way to circumvent these conflicting demands. Moreover, as a consequence of equation (1), the radiation from the surrounding environment has to be controlled or at least characterized. In the following, the discussion is specialized to the specific set-up that has been designed to allow for the simultaneous kinematic and thermal measurement.

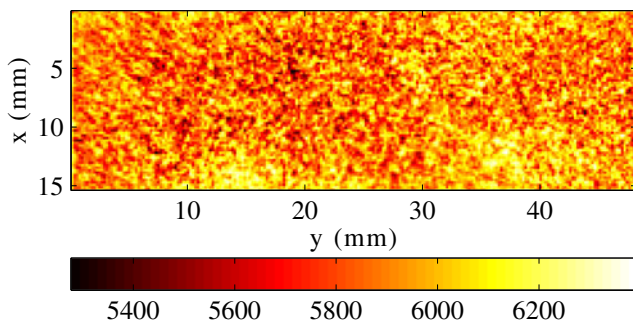


Fig. 1 Raw IR image of the speckled sample in a steady uniform state and at ambient temperature (around 26°C, $\Delta T_{\text{sample/surrounding}} \approx 20^\circ\text{C}$). The grey level is expressed in Digital Level (DL) over a total range of $2^{14} \approx 16,000$ DL corresponding to the temperature range [5°C ; 60°C]

Designed Coating and Specific Measurement Set-up

In the specific case of the Ni-Ti sample studied in Section “[Application: Tensile Test on Ni-Ti SMA](#)”, such a surface is prepared as follows: the specimen is first electro-chemically polished, giving a very weak emissivity ($\epsilon_{\text{metal}} \approx 0.1$); a mist of fine droplets of high emissivity black paint ($\epsilon_{\text{paint}} \approx 0.97$) is then sprayed onto the surface so that it does not cover the entire surface (see Fig. 1).

Thus, in the covered areas, the measured radiation intensity gives access to the local temperature, whereas

the uncovered area is strongly influenced by the surrounding radiation. In order to be able to interpret the local R_p , the surrounding radiation, Φ , has to be controlled. The metallic nature of the material and its very good surface finish implies that most of this surrounding radiation comes from a specular reflection over the surface. This observation dictates the specific geometry that was chosen for our experimental set-up, as shown in Fig. 2(a). An extended black body at a constant and uniform temperature T_{surr} is positioned so that it would be imaged by the IR camera if the sample was a mirror. It consists of a rectangular prismatic tank ($200 \times 300 \times 100 \text{ mm}^3$) entirely filled with ice cubes and water. Its front face is coated with a homogeneous paint of high emissivity. The temperature of this face is about $T_{\text{surr}} \approx 4^\circ\text{C}$ with a standard deviation $\leq 0.3^\circ\text{C}$. Therefore, as a good approximation the surrounding radiation can be treated as a uniform quantity

$$\Phi \approx \sigma_{SB} \cdot T_{\text{surr}}^4 \quad (3)$$

Provided the regulated temperature, T_{surr} , is much lower than that of the sample, the speckled sample will appear as heterogeneous in the IR images as shown in Figs. 1 and 2(b).

Figure 2(b) was recorded during a Ni-Ti SMA tensile test which is detailed in Section “[Application: Tensile Test on Ni-Ti SMA](#)”. One notices clearly a localized temperature elevation, indicative of a phase transformation. It is thus obvious that temperature field infor-

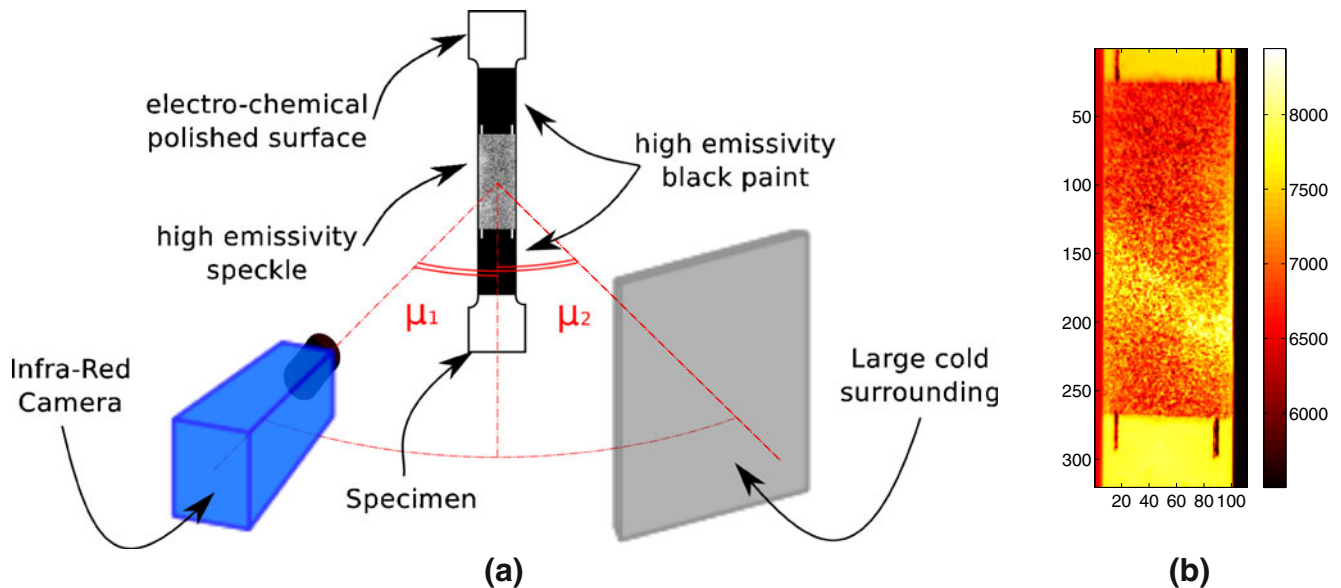


Fig. 2 (a) Experimental set-up showing the relative position of the IR camera, the specimen surface and the extended black body. (b) Infrared raw picture observed during tensile test on

Ni-Ti SMA showing the speckled specimen face undergoing a strain and heating localisation

mation can be inferred from the IR images. However, due to the non-uniform emissivity, this inference is less direct than in the traditional method: a prior coating calibration has to be performed.

Prior Coating Calibration

A first measurement of the natural cooling of the sample is needed to calibrate the coating and the related experimental set-up. To this end, the sample is mounted in the testing machine and the imaging devices are set up and adjusted for the measurement as shown Fig. 2(a). From a practical point of view, the camera and the extended black body are positioned on either side of the normal of the observed surface, with a small angle μ equal on both sides ($\mu_1 = \mu_2 \simeq 14^\circ$). The sample is maintained by hydraulic grips in the MTS uniaxial 100 kN testing machine. To obtain as uniform a cooling as possible, the sample is only positioned in the lower grip, with the hydraulic supply turned off. Thus no hydraulic heat is transmitted to the sample. Moreover insulating plastic sheets are inserted between grips and jaws.

The sample is heated up to $\simeq 65^\circ\text{C}$ by the use of powerful convective heaters. This process induces a rather homogeneous temperature. In order to have reliable information on the temperature distribution, the back side of the sample is covered with a high emissivity black paint. A gold coated first surface mirror, (Edmunds Optics Techspec series), is set up just behind the specimen. This kind of mirror has a single reflective

surface (the first one) and thus impedes spurious multiple reflections. Moreover, this reflection is very high in the middle wave IR because of its coating. Hence, the back side of the specimen is imaged by the camera as in a direct configuration, except that it is slightly out-of-focus. An independent experimental study has shown that the temperatures estimated through the IR mirror are indeed reliable. Figure 3(a) shows the set up during calibration recording. Figure 3(b) is a raw IR image of the sample front and back sides. The recorded cooling starts around 61°C and finishes around 26°C . A relevant range of temperature should coincide with the one observed on the sample during the actual test. In order to obtain a valid calibration, the IR film has to be recorded with the exact same adjustments as for the mechanical test. Images show that the temperature field is quite homogeneous. At a high temperature, a longitudinal gradient is nevertheless observable which vanishes close to the ambient temperature, as shown in Fig. 4. It allows us to assume the temperature to be uniform at the end of the cooling. This assumption provides a reference point for the description of the grey level evolution.

The calibration process consists in extracting the relevant parameters describing the variation of grey level of each pixel during cooling. Section “[Texture Evolution with Temperature Over a Small Test Area](#)” investigates this variation over an area small enough to be considered as having a uniform temperature field. Once the correspondence is found, it is applied to the whole sample in Section “[Global Texture Evolution with Temperature](#)”. Last, the conversion from apparent

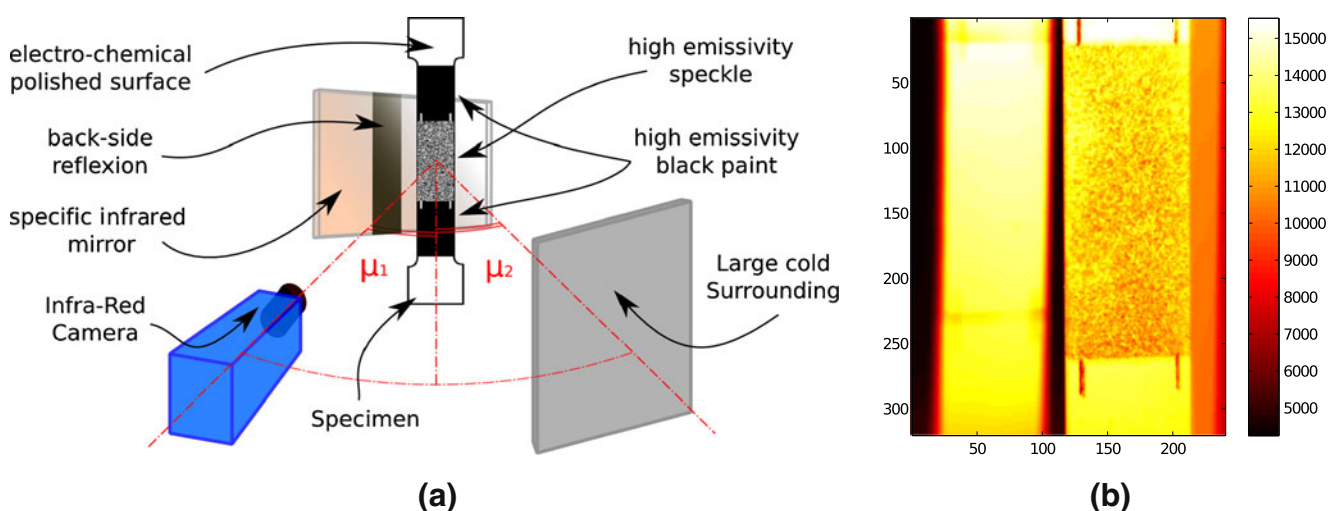


Fig. 3 (a) Experimental set-up during calibration: specific IR mirror is set up just behind the sample (b) infrared raw picture of the front side and back side of the sample at $T_{\text{mean}} \simeq 58.5^\circ\text{C}$

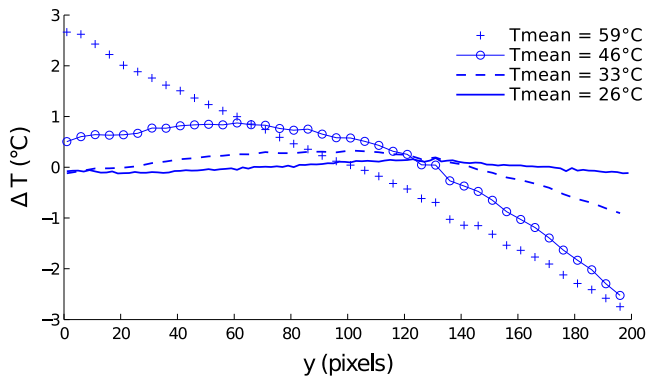


Fig. 4 Longitudinal profile of deviation from the mean temperature measured on the back side

to real temperature is detailed in Section “[Conversion from Apparent to Real Temperature](#)”.

Texture Evolution with Temperature Over a Small Test Area

As seen in the previous subsection, the grey level of each material point, $f(x, T)$ expressed in Digital Level (DL), evolves with the temperature variation. In order to correctly describe this evolution, the sample’s cooling is observed. In spite of the aforementioned experimental cautions, a small temperature gradient is present along the longitudinal direction during most of the cooling period, due to the boundary conditions of the problem (the cooling of the sample is mainly due to the heat flux toward the grips). However, at the end

of this period the temperature total dispersion over the entire sample is less than 0.3°C (see Fig. 4).

To investigate the relationship between grey level and local temperature, one chooses a small area (10×10 pixels i.e. $2.1 \times 2.1 \text{ mm}^2$) of the sample Ω over which the temperature gradient can be neglected. Considering that the average grey level over this area gives a rough idea of the temperature, one defines an apparent temperature through the mean value of the grey level over the Ω area :

$$\Theta = \langle f(x, T) \rangle_{x \in \Omega} . \tag{4}$$

Figure 5(a) shows the typical exponential decrease of this apparent temperature during natural cooling. Initial apparent temperature is less than 65°C since the average emissivity over Ω is much lower than 1.

For the sake of simplicity, it is first assumed that the sample is not moving over time so that each pixel refers to the same sample surface point. Obviously, thermal expansion may violate this assumption but its importance will be checked hereafter. A plot of the grey level variation of each pixel versus the apparent temperature (as shown in Fig. 5(b)), shows that a linear evolution is quite convincing although the slope and offset of each line is dependent on the chosen pixel. The affine relation between $f(x, t)$ and Θ is written

$$f(x, t) = a\Theta + b \tag{5}$$

where a and b are respectively the slope and offset which characterize each pixel’s dependence with the apparent temperature.

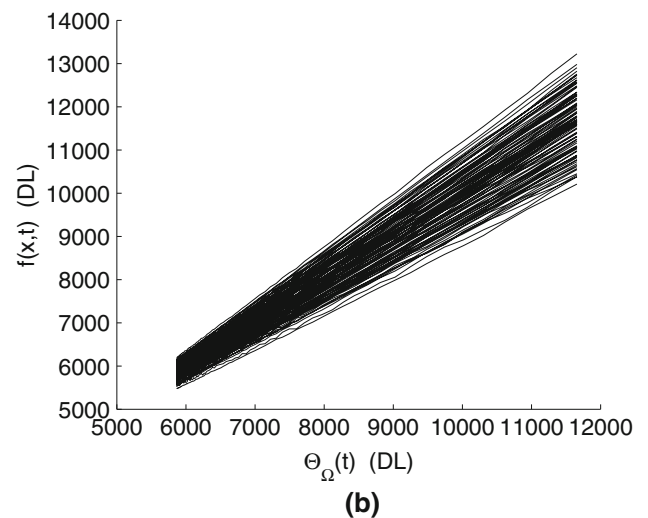
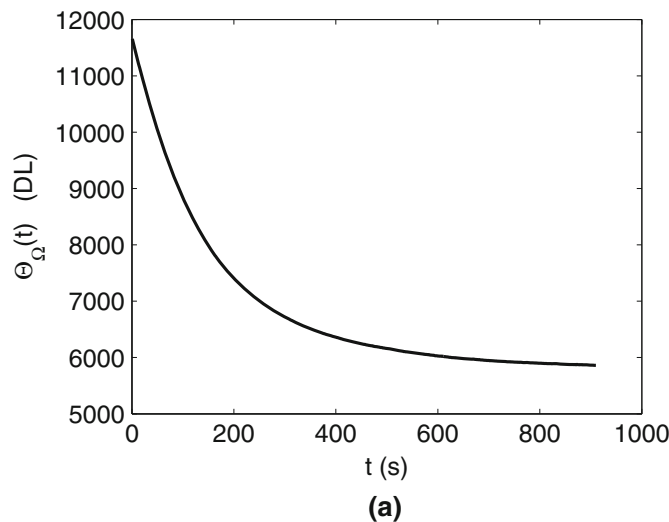


Fig. 5 (a) Apparent temperature evolution Θ of the Ω area as a function of time t and (b) grey level evolution of some pixels as a function of apparent temperature



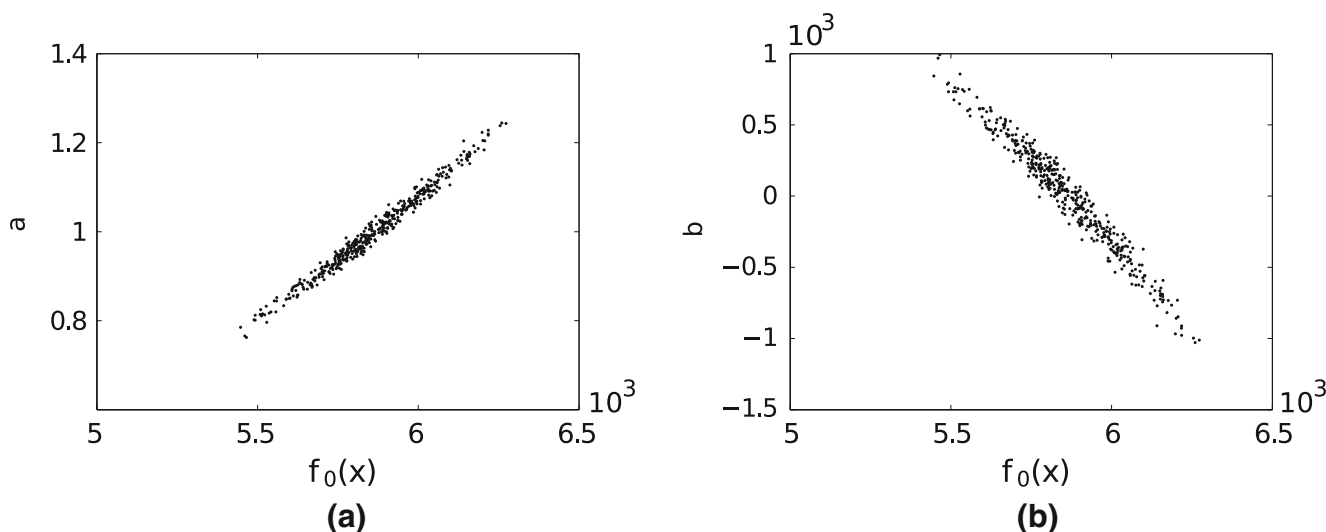


Fig. 6 (a) slope and (b) offset of the grey level’s dependence on temperature as a function of the reference grey level, $f_0(\mathbf{x})$

One may assume that a and b are linked to the local emissivity of the surface. The final image is defined as a reference image. It displays a temperature, denoted as T_0 but “measured” through Θ_0 , and each pixel is characterized from its reference grey level: $f_0(\mathbf{x}) = f(\mathbf{x}, T_0)$. The quantities a and b are shown in Fig. 6 as a function of the reference grey level $f_0(\mathbf{x})$. These quantities are again linearly dependent on $f_0(\mathbf{x})$. It is noteworthy that, as expected, a increases with f_0 since high values of f_0 correspond to high emissivity (remember that the temperature of the black body is lower than that of the sample). The relation between f , $f_0(\mathbf{x})$ and Θ now reads

$$f(\mathbf{x}, t) = (\alpha_1 f_0(\mathbf{x}) + \alpha_2)\Theta + (\beta_1 f_0(\mathbf{x}) + \beta_2) \quad (6)$$

When the apparent temperature reaches $\Theta = \Theta_0$, we expect $f(\mathbf{x}, t) = f_0(\mathbf{x})$ hence

$$\begin{aligned} \alpha_1 \Theta_0 + \beta_1 &= 1 \\ \alpha_2 \Theta_0 + \beta_2 &= 0 \end{aligned} \quad (7)$$

so that f can be simplified to

$$f(\mathbf{x}, t) = f_0(\mathbf{x}) + (\alpha_1 f_0 + \alpha_2)(\Theta - \Theta_0) \quad (8)$$

Moreover, the very definition of the apparent temperature, $\Theta = \langle f(\mathbf{x}, t) \rangle_x$, imposes

$$\Theta = \Theta_0 + (\alpha_1 \Theta_0 + \alpha_2)(\Theta - \Theta_0) \quad (9)$$

or $\alpha_2 = 1 - \alpha_1 \Theta_0$.

It is to be noted that for a particular apparent temperature, denoted as Θ_x and associated with T_x temperature

$$\Theta_x = \Theta_0 - \frac{1}{\alpha_1} \quad (10)$$

the sample image is easily computed to be

$$f(\mathbf{x}, T_x) = \Theta_x \quad (11)$$

for all \mathbf{x} . In other words, the inhomogeneous emissivity texture vanishes and the image should appear as uniform. From the above description of our set-up, the interpretation of this temperature is straightforward: it corresponds to that of the surrounding being reflected on the sample. Indeed, from equation (1), when the sample and surrounding temperatures become equal, the image is that of an ideal homogeneous black body. The final expression of the image for an arbitrary temperature field thus reads

$$f(\mathbf{x}, t) = \Theta(t) + \frac{(\Theta_x - \Theta(t))}{(\Theta_x - \Theta_0)}(f_0(\mathbf{x}) - \Theta_0) \quad (12)$$

where time and space dependencies have been decoupled.

Finally, this procedure is very redundant as the only quantity to be determined is Θ_x . Therefore, we may check the validity of the proposed form from the computation of the residual field, η , equal to the difference between the left and right member of equation (12). Figure 7 shows that residual is low, except for the beginning of the cooling, when the temperature is still high. One possible origin of such a deviation is the motion of the sample in front of the camera due to thermal dilatation. Thus, for a small amplitude motion \mathbf{U} , η should be equal to

$$\eta(\mathbf{x}, t) = \frac{(\Theta_x - \Theta(t))}{(\Theta_x - \Theta_0)}(\nabla f_0(\mathbf{x}) \cdot \mathbf{U}) \quad (13)$$

This relation is used to evaluate the displacement, \mathbf{U} , that is shown in Fig. 8 as a function of time. It is

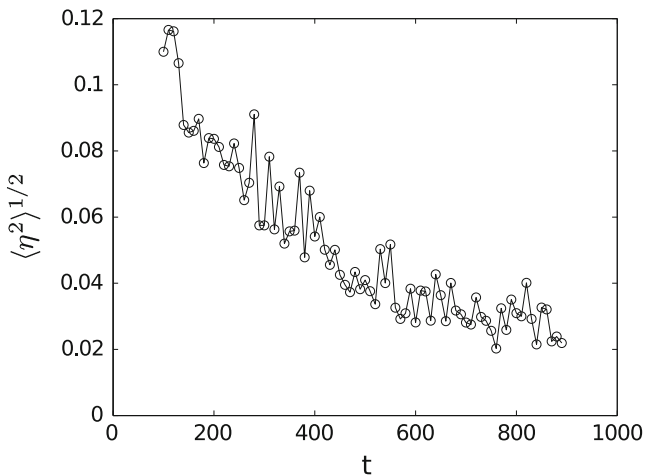


Fig. 7 Dimensionless residual as a function of time. The decay of the residual can be at least partly attributed to the displacement induced by thermal expansion

observed that only the first images violate the initial hypothesis of a fixed sample by more than one tenth of a pixel. One points out that the evolution of U_x with time is similar to the one of the apparent temperature [Fig. 5(a)] and that the magnitude of this displacement is in good agreement with the thermal expansion.

The above analysis allows one to probe the consistency of the observations with the expected behaviour from our experiment design. However, only a small zone is analysed here because of the needed assumption of a negligible temperature gradient over the zone.

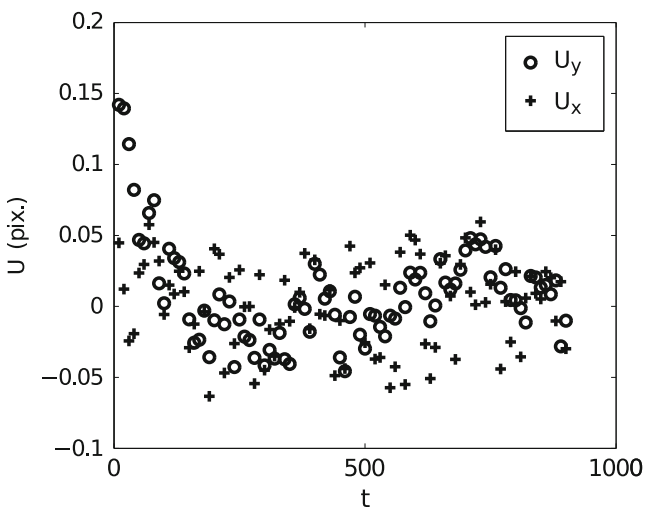


Fig. 8 Rigid body motion amplitude (expressed in pixel) versus time t in both directions. Only the first few images show a significant longitudinal displacement of the studied small zone located over the sample mid-line. The transverse displacements are equal to zero

Global Texture Evolution with Temperature

In order to base our analysis over the entire sample surface, it is proposed to extend the above procedure to a spatially varying temperature field. Of course, the temperature field cannot be assumed to be arbitrary, and some regularization assumptions have to be made. It is assumed that the temperature field can be fitted by a low order polynomial in the spatial coordinates. A fourth order was chosen so as to introduce enough flexibility, but a reduction to third order had no observable consequences and hence, this regularization is considered as reliable. The equivalent of the apparent temperature Θ is now given at any point and time as the value of the polynomial regression of the grey levels. Apart from the resulting spatial dependence of Θ , all the above procedure can be followed. Although the determination of the apparent temperature Θ (with a known estimate of Θ_x), and the evaluation of Θ_x (for a known Θ field) are both linear problems, the joint determination is not. Therefore an iterative two-step procedure was followed. The first step consists of adjusting the Θ field from the 4th-order polynomial fit of the guessed temperature

$$\Theta_{\text{guess}} = \frac{\Theta_0 \cdot (f - \Theta_x) - \Theta(f - f_0)}{(f_0 - \Theta)} \quad (14)$$

The second step consists of correcting the Θ_x value according to

$$\Theta_x = \frac{\langle (\Theta \cdot f_0 - \Theta_0 \cdot f) (\Theta - \Theta_0 + f_0 - f) \rangle_{x,t}}{\langle (\Theta - \Theta_0 + f_0 - f)^2 \rangle_{x,t}} \quad (15)$$

These two steps are repeated until convergence. Convergence is set when a norm of the incremental correction on Θ reaches a small parameter value, here 10^{-8} . This very conservative value is chosen because convergence is actually extremely fast, and very few iterations are needed.

Conversion from Apparent to Real Temperature

Last, the apparent temperature Θ has to be converted into the real temperature T . To do so, one exploits the two areas near the ends of the specimen which are covered by a uniform high emissivity paint (see Fig. 2(b)). These two areas allow for a direct local temperature measurement in celsius degrees since, before the cooling phase, the camera has been accurately calibrated using a black body whose emissivity, as the black paint one, is close to 1. The camera calibration is standard, and is briefly described in Section “[Application: Tensile Test on Ni-Ti SMA](#)”.

A low order polynomial fit of the temperature over each of these areas is first computed to lower noise influence. The polynomial fit of the apparent temperature on the gauge zone is then extended to both ends of the specimen. The RMS difference between the apparent and the true temperatures on the two areas is finally minimized during cooling time by multiplying the apparent temperature by a constant. This emissivity correction coefficient value is typically about 1.3, i.e., the average emissivity of the IR speckle is about $1/1.3 \simeq 0.75$. The previously estimated value of Θ_{\times} (in DL) turns out to be equivalent to the true temperature value of $T_{\times} = 8.1^{\circ}\text{C}$. This value is in good agreement with the temperature of the extended black body ($\approx 4^{\circ}\text{C}$) plus a small contribution of the rest of the surrounding.

Mathematical Formulation and Numerical Algorithm

The grey level evolution under a temperature change—and only a temperature change—is described (see Section “Prior Coating Calibration”) by equation (12). In the most general case, the image of a deformed specimen, $g(\mathbf{x})$, can be related to the reference picture, $f_0(\mathbf{x})$, chosen to be the one captured at the end of the thermal calibration step (i.e., the isotherm state at temperature T_0)

$$g(\mathbf{x} + \mathbf{u}(\mathbf{x})) = \Theta(\mathbf{x}) + \frac{\Theta_{\times} - \Theta(\mathbf{x})}{\Theta_{\times} - \Theta_0} (f_0(\mathbf{x}) - \Theta_0) . \quad (16)$$

The goal is here to determine both the displacement fields $\mathbf{u}(\mathbf{x})$ and the temperature field $\Theta(\mathbf{x})$. They are computed jointly from a weak formulation of the above law, through the minimization of the following objective function

$$\begin{aligned} \mathfrak{R}[\mathbf{u}, \Theta] &= \int \left(g(\mathbf{x}') - f_0(\mathbf{x}) - \frac{\Theta(\mathbf{x}) - \Theta_0}{\Theta_{\times} - \Theta_0} \cdot (\Theta_{\times} - f_0(\mathbf{x})) \right)^2 d\mathbf{x} \end{aligned} \quad (17)$$

where $\mathbf{x}' = \mathbf{x} + \mathbf{u}(\mathbf{x})$.

The global DIC approach introduced in [11] is extended to the generalized form of the brightness conservation. Both displacement and temperature fields are decomposed onto a unique basis of function

$$\begin{aligned} \mathbf{u}(\mathbf{x}) &= \alpha_{ij} \Phi_i(\mathbf{x}) \mathbf{e}_j \\ \Theta(\mathbf{x}) &= \Theta_{\times} + \alpha_{i3} \Phi_i(\mathbf{x}) \end{aligned} \quad (18)$$

where $1 \leq i \leq N_k$ represents the node numbering, $1 \leq j \leq 2$ gives the displacement direction, while $j = 3$

refers to the temperature. Moreover the unknown to be determined are hence gathered into a single vector $\boldsymbol{\alpha} = \{\alpha_{ij}\}$.

The algorithm proceeds through successive linearization of the bracketed expression in the above objective function around the current determination of the (\mathbf{u}, Θ) field. A corrected deformed image at step n of the algorithm, using the determined $\boldsymbol{\alpha}^{(n)}$, is

$$g^{(n)}(\mathbf{x}) = g(\mathbf{x}'^{(n)}) - \alpha_{i3}^{(n)} \Phi_i(\mathbf{x}) . \quad (19)$$

Then, the additional correction in $\boldsymbol{\alpha}$, denoted as $\delta\boldsymbol{\alpha}^{(n)}$, is computed from the linearized expression in the objective function

$$\begin{aligned} \mathfrak{R}_{lin}[\boldsymbol{\alpha}] &= \int_{\mathcal{D}} \left(g^{(n)}(\mathbf{x}) - f_0(\mathbf{x}) - \delta\alpha_{ij}^{(n)} \Phi_i(\mathbf{x}) \partial_j f_0(\mathbf{x}) \right. \\ &\quad \left. - \delta\alpha_{i3}^{(n)} \Phi_i(\mathbf{x}) \cdot \frac{f_0(\mathbf{x}) - \Theta_{\times}}{\Theta_0 - \Theta_{\times}} \right)^2 d\mathbf{x} . \end{aligned} \quad (20)$$

This minimization leads to the following linear system

$$[\mathbf{M}]\{\delta\boldsymbol{\alpha}^{(n)}\} = \{\delta\boldsymbol{\beta}^{(n)}\} \quad (21)$$

in the expression of which it is convenient to introduce the three component vector \mathbf{G} ,

$$\mathbf{G} = \begin{pmatrix} \partial_1 f_0(\mathbf{x}) \\ \partial_2 f_0(\mathbf{x}) \\ \frac{f_0(\mathbf{x}) - \Theta_{\times}}{\Theta_0 - \Theta_{\times}} \end{pmatrix} . \quad (22)$$

The $3N_k \times 3N_k$ matrix $[\mathbf{M}]$ consists in 3×3 blocks

$$[\mathbf{M}]_{ij} = \int_{\mathcal{D}} (\mathbf{G} \cdot \Phi_i) \otimes (\mathbf{G} \cdot \Phi_j) d\mathbf{x} \quad (23)$$

and the second member $\boldsymbol{\beta}$ is a $3N_k$ vector consisting in N_k blocks of size 3

$$\{\delta\boldsymbol{\beta}^{(n)}\}_i = \int_{\mathcal{D}} (\mathbf{G} \cdot \Phi_i)(g^{(n)} - f_0) d\mathbf{x} \quad (24)$$

and finally, the amplitudes are updated according to

$$\boldsymbol{\alpha}^{(n+1)} = \boldsymbol{\alpha}^{(n)} + \delta\boldsymbol{\alpha}^{(n)} . \quad (25)$$

This completes one iteration step of the algorithm.

This formulation is the most efficient since the deformed image is corrected rather than the reference one. This allows for having a fixed expression for the matrix $[\mathbf{M}]$, independent of the iteration number. This is important for computation efficiency as the simple construction of this matrix requires a significant amount of time (pixelwise spatial integrations are needed). Moreover, for a long temporal sequence of images g , the very same matrix is to be used. It is to be emphasized that $\Theta(\mathbf{x})$ and $\mathbf{u}(\mathbf{x})$ are indeed determined jointly, through a unique computation of the $\boldsymbol{\alpha}$ vector.



Numerical Algorithm Uncertainty

Three analysis campaigns are carried out to assess the displacement, strain and temperature measurement uncertainties. For each quantity, different uniform fields are artificially imposed to the same reference image (the last one from the calibration procedure record) to generate test images. The IRIC algorithm is then applied separately to each of the test images and the reference one. Four mesh sizes are used from 24×24 pixels down to 6×6 pixels. Between each mesh size, the $[M]$ matrix is not fully computed but only updated from the previous mesh size computation result, in order to reduce convergence time and error. Last, the gap between the computed and prescribed field is calculated. Two indicators are used to assess the measurement accuracy: the systematic error (mean error to the prescribed value) and the standard uncertainty (standard deviation of the computed field).

Displacement Uncertainty

Nine test images are generated by applying uniform sub-pixel displacements, from 0.1 pixels to 0.9 pixels. Thanks to the mesh size top-down analysis, the systematic error is fairly constant whatever the mesh size be. For sub-pixel prescribed displacement the mean error is less than 0.05 pixel for 12×12 mesh size. As expected, Fig. 9 shows that the finer the mesh, the larger the uncertainty. The uncertainty value is independent of the mean measured displacement, and so is the measured

thermal field which stays uniform and constant. The standard deviation of the computed temperature field is less than 5×10^{-2} pixels, apart from boundary elements where values are slightly more important.

Strain Uncertainty

Test images are now generated applying artificial uniform strain fields, on both sides of the vertical mid-line, from 10^{-4} to 16×10^{-4} . Figure 10 shows first that the strain is globally overestimated (mean systematic error around 2×10^{-4} for these prescribed strains). Second, both accuracy indicators are more dependant on the mesh size, probably because of the strain calculation method. The strain uncertainty is nonetheless appreciable, ranging from 10^{-4} to 10^{-3} for mesh size 12×12 . Once more the temperature field is not affected by the prescribed strain. The correlation residue fields reflect the prescribed displacement field, but the maximal error value remains very low (20 grey levels for an original grey level range around 1,000).

Temperature Uncertainty

Test images are last generated so that the grey level of each pixel is modified in agreement with the proposed formulation [equation (12)] to simulate temperature increase from 0.1°C to 0.9°C . Figure 11 shows that mesh size does not influence the temperature measurement uncertainty, which globally ranges from 10^{-4} to 10^{-3}°C . These noticeably low values correspond to

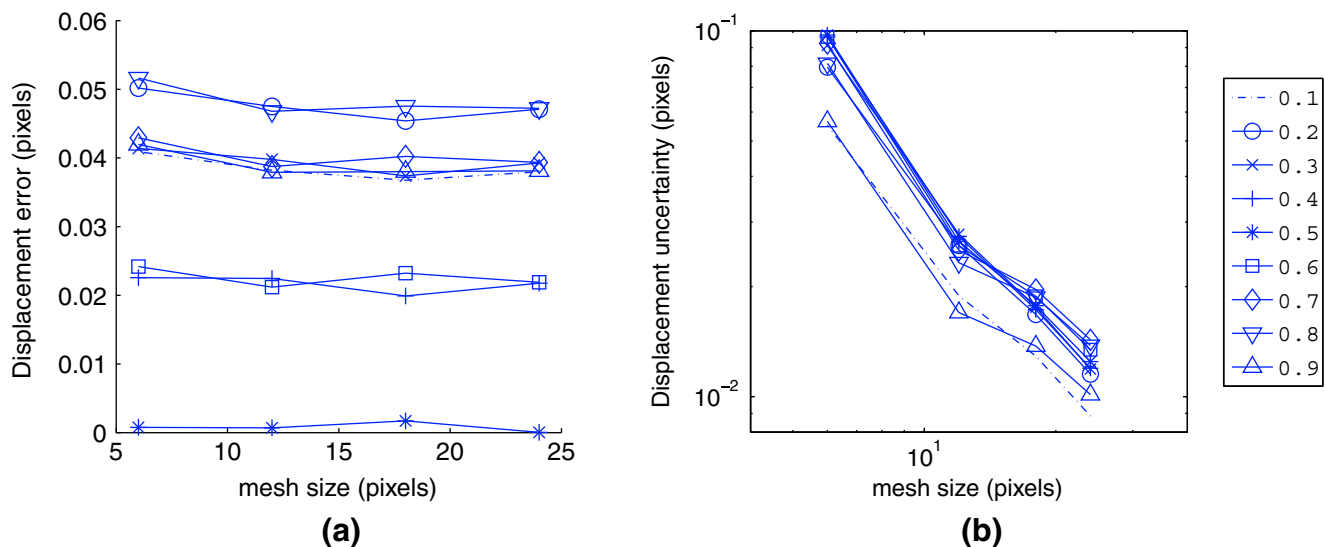


Fig. 9 Systematic error (a) and standard uncertainties (b) for each prescribed displacement as a function of the mesh size

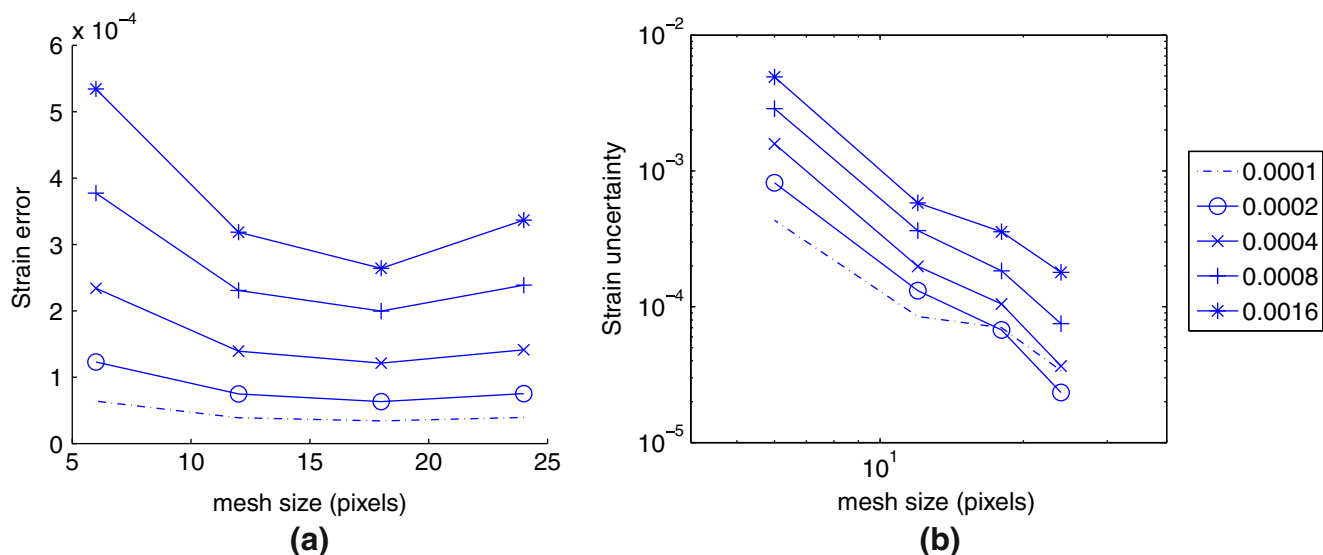


Fig. 10 Systematic error (a) and standard uncertainties (b) for each prescribed strain as a function of the mesh size

the numerical errors introduced by the IRIC algorithm. They must not be misinterpreted as the real temperature measurement uncertainty, which is highly dependent on the camera’s own Noise Equivalent Thermal Difference, around $2 \times 10^{-2} \text{ }^\circ\text{C}$ in the present case. The kinematic fields are not influenced by the prescribed temperature field.

Last, it is interesting to compare IRIC to its “father” DIC software Correli-Q4 [11], from which this IRIC method is derived. The exact same set of test images are used to assess Correli-Q4 own performances.

The displacement uncertainty is only around 2.5 time smaller. Concerning strain uncertainty, both standard uncertainty and systematic error are of the same order of magnitude than IRIC ones ($10^{-4} \leq \sigma_\epsilon \leq 10^{-3}$ and $10^{-5} \leq \delta_\epsilon \leq 5.10^{-4}$). It means that the kinematic accuracy is not so much deteriorated, though the IRIC degree of freedom number is more important since it affords both kinematic and thermal fields. These uncertainty investigations tend to prove that the used top-down method also provides a good robustness to the proposed algorithm.

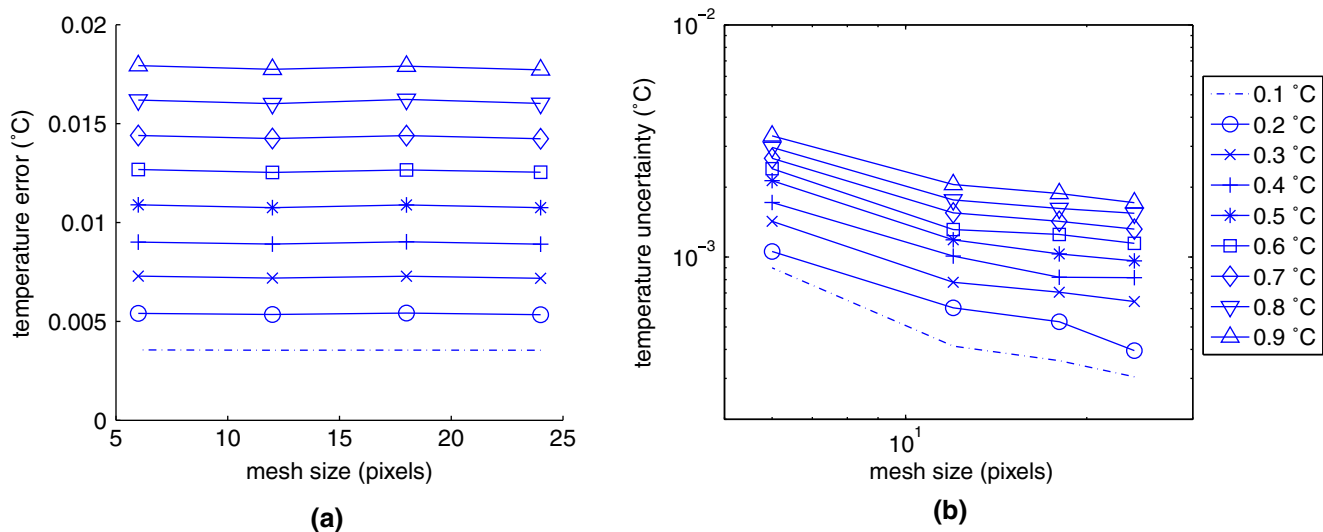


Fig. 11 Systematic error (a) and standard uncertainties (b) ($^\circ\text{C}$) for each prescribed heating as a function of the mesh size

Application: Tensile Test on Ni-Ti SMA

Localisation in Ni-Ti Based SMA

Specific behavior of SMA is due to a martensitic solid-solid phase transformation which can be activated either by mechanical loading or temperature variations. The high temperature phase is called austenite whereas the low temperature phase is known as martensite. Among the various consequences of this phase change, the so called superelastic behavior is observed during mechanical loading at high temperature: a specimen, elongated in an apparently plastic way, gets back to its initial shape.

Descriptions of the strain localisation are numerous in literature [12, 13] essentially on Ni-Ti samples of various shapes (flat-bone shaped, thin tubes, wires) loaded in tension. One may notice some of their particularities. First, localisation patterns generally form bands for flat samples [14] and helices for thin tubes [8, 15–17], with an inclination angle of 55° with respect to the tension direction. Second, the nucleation of a single or multiple band(s) and their propagation are sensitive to the imposed global strain rate [6]. Last, values of von Mises equivalent strain into bands are observed to be of the order of 3.5% whereas the equivalent strain outside the bands remains lower than 1.5% [14].

From a thermal point of view, the sample global temperature elevation may reach typical values of 20°C , due to the transformation latent heat, while heterogeneity magnitude is about 8°C , due to localization during tensile tests. These values obviously depend also on the specimen geometry and environment [18].

This combination of strong strain localization and thermal heterogeneity evolution makes Ni-Ti SMA a perfect candidate to demonstrate the potential of the IRIC method.

Testing Set-up and Material Description

The material used for the test has a Ti-Ni 55.4 wt% composition (commercial name SE508) and is produced by Nitinol Devices and Components (Fremont, California, USA). Flat-bone shaped samples are formed by Nitifrance (Lury-sur-Arnon, France). The forming consists mainly in a cold-rolling followed by a heat treatment of 2 minutes at 480°C in a salt bath. Samples are flat bone shaped, their cutting was performed by electro-erosion and followed by mirror polishing. They have a rectangular section of $20 \times 2 \text{ mm}^2$ and a gauge zone length of 120 mm.

The transformation temperatures of the sample are estimated thanks to Differential Scanning Calorimetry

(DSC) measurement : austenite start $A_s = 13^\circ\text{C}$, austenite finish $A_f = 23^\circ\text{C}$, martensite start $M_s = 21^\circ\text{C}$ and martensite finish $M_f = 8^\circ\text{C}$. No trace of rhombohedral phase (R-phase) is observed for this specific forming and heat treatment.

Test is performed on the previously described testing machine. Loading force and global displacement are measured. Loading is displacement controlled, with rate set to 2 mm/min and a maximum displacement value of 10 mm. The test is performed at ambient temperature (25°C). These test conditions were chosen to be consistent with previous test results, performed on similar samples [19].

Our IR camera (Jade III produced by CEDIP®) allows us to obtain images with a 320×240 pixels spatial resolution, an acquisition frequency of 100 Hz and an integration time of $930 \mu\text{s}$. In the present experiment, the physical size of a pixel is about $210 \mu\text{m}$. The framing is chosen so that bands can be tracked on the major part of the gauge length, at the expense of the resolution along the width of the specimen.

In order to achieve the conversion from measured flux by the camera to Celsius Degree ($^\circ\text{C}$), the camera itself has to be calibrated independently of the rest of the experimental set-up. A standard 2-points Non-Uniformity-Correction (NUC) [20] and a polynomial calibration are performed. Thirteen IR pictures of an extended black body are recorded each 5°C , from 0°C to 60°C . This range, nearly centered on the ambient temperature, contains the surrounding temperature and is sufficiently extended to cover the maximum temperature expected in the experiment where the Ni-Ti AMF martensitic phase transformation occurs. NUC is calculated with two images at 1/4 and 3/4 of

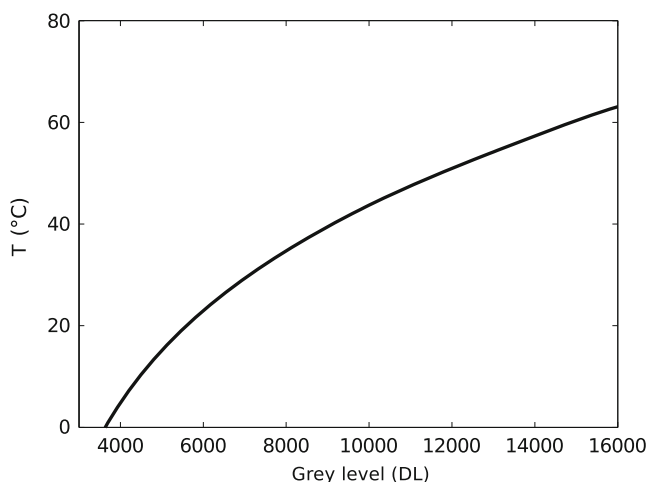


Fig. 12 Camera seventh order calibration for conversion of Digital Levels (DL) to Celsius Degrees ($^\circ\text{C}$)

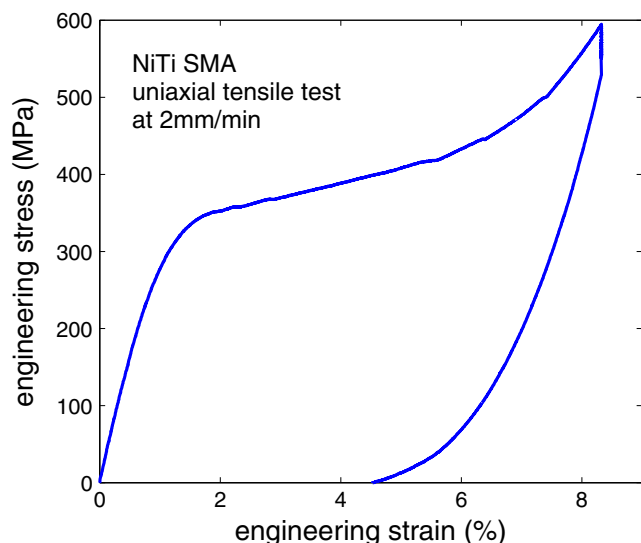


Fig. 13 Stress-strain curve for the analyzed test

the temperature range. The mean Digital Level versus black body temperature is fitted by a seventh order polynomial as shown in Fig. 12.

Results and Interpretation

The obtained global stress—engineering strain curve is given in Fig. 13. Engineering strain means here actuator

displacement relative to the initial length of the sample. The observed plateau is specific to superelastic behavior, *i.e.* stress induces austenite to martensite transformation.

The IR film of the whole tension test is post-processed using the numerical procedure described in Section “**Mathematical Formulation and Numerical Algorithm**”. The computation of 226 images (region of interest 73×239 pix.) lasts about 20 minutes on a standard laptop computer. We now present the analysis of a single IR image (no time averaging) extracted from the plateau regime at the onset of the first visible shear band, at about 2% engineering strain. The size of the element is chosen to be $\ell = 12$ pixels (about 2.5 mm) wide. Larger elements smear out the shear band over a larger region, whereas smaller ones display a significant amount of fluctuations.

Figure 14 shows (a) the region of interest of the reference image (prior to loading, after calibration cooling period) as imaged with the IR camera and (b) a similar region of the specimen under load at the onset of the first localization band.

Figure 14(c) shows image (b) after the numerical algorithm procedure. Image (b) is corrected by the measured displacement field and the temperature elevation, and is to be compared with (a). The difference (or the residual) between this corrected image and the reference one is shown in (d) with the same gray level

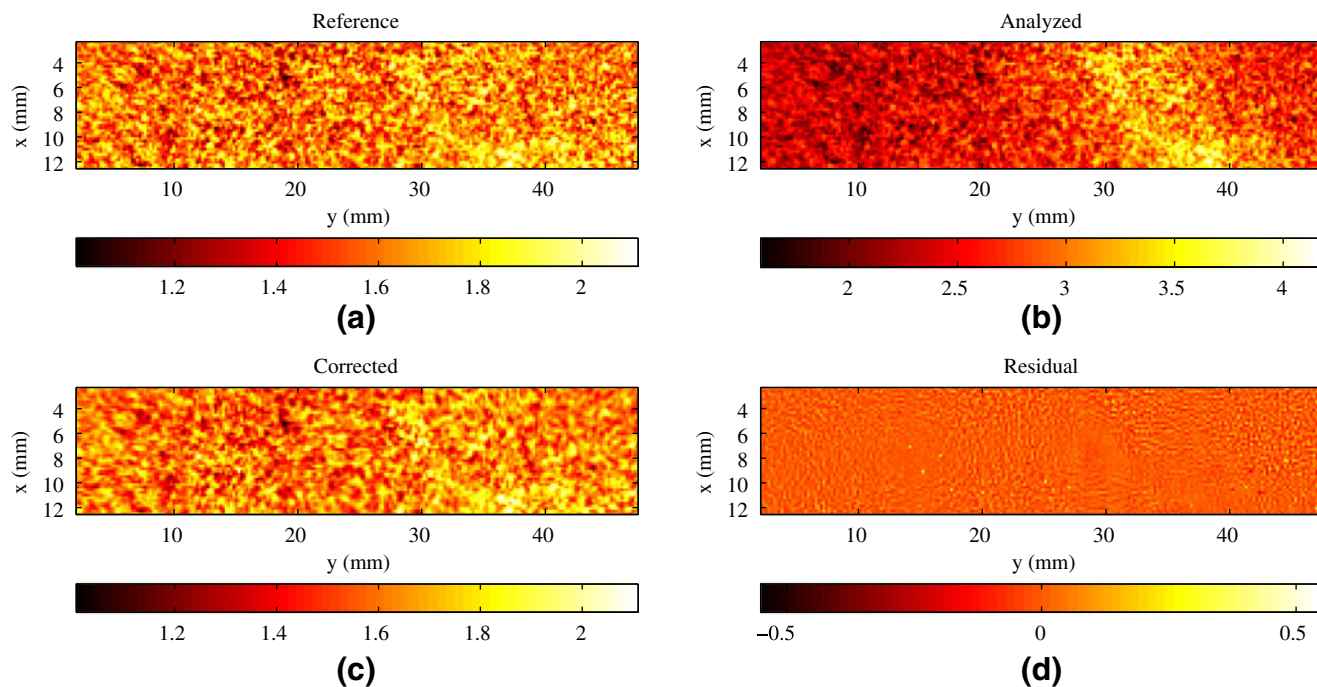


Fig. 14 (a) Reference and (b) deformed images. The corrected deformed image and its difference with the reference, (called the residual), are shown respectively in (c) and (d)

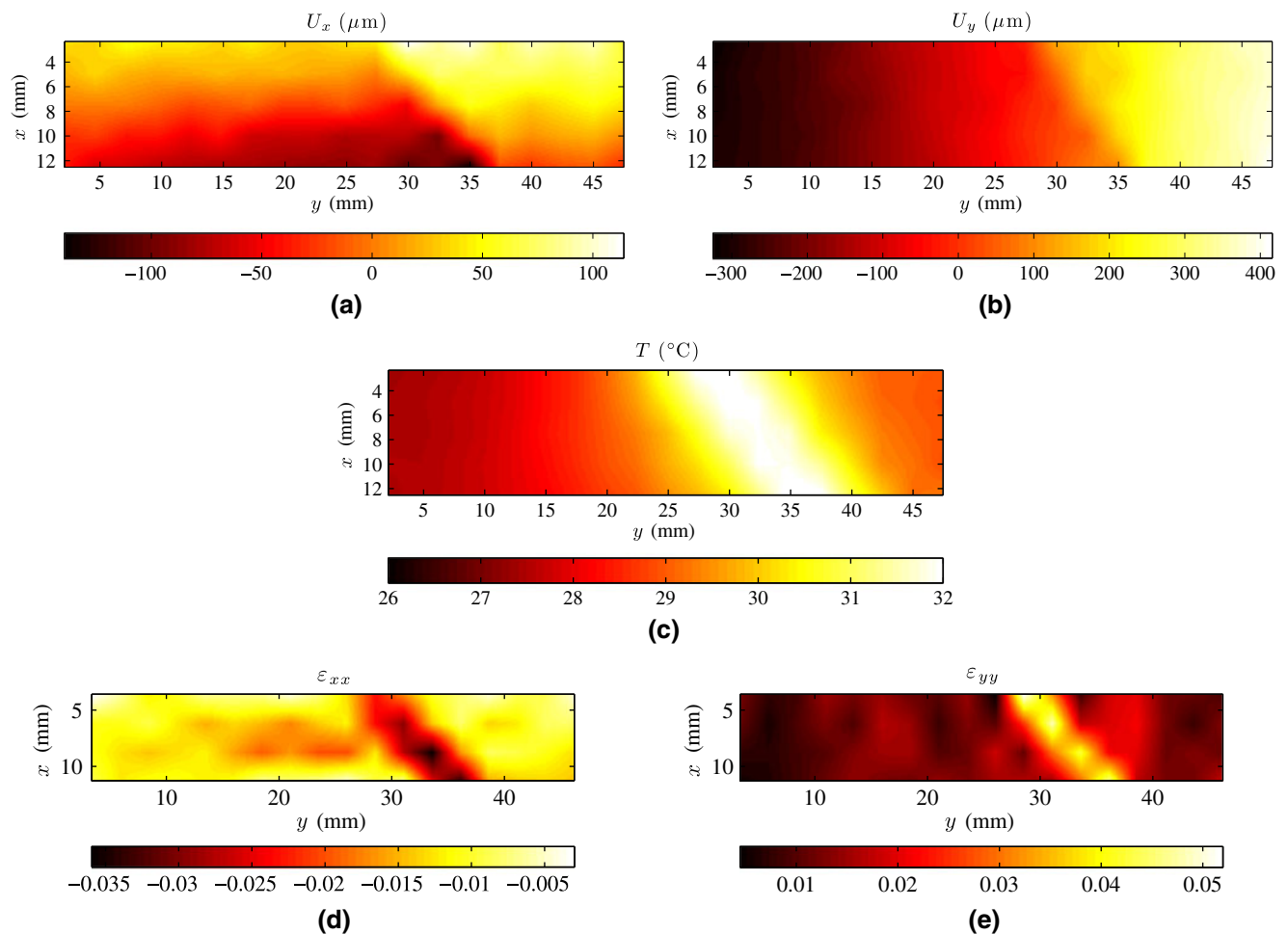


Fig. 15 (a) Transverse and (b) longitudinal displacements in micrometers, without rigid body motion. (c) Temperature field in Celsius degrees. (d) and (e) show respectively the transverse (ϵ_{xx}) and longitudinal (ϵ_{yy}) strain fields

dynamic range as the reference image. The uniformity of this difference signals a successful registration of the images. It is to be emphasized that the obvious temperature rise along the transformation band in (b) is mostly erased after the correction (c).

The temperature field obtained from the infrared Image Correlation procedure outlined above is shown in Fig. 15(c). The temperature field has been converted to Celsius degree. The estimated temperature rise within the shear band is about 4°C above that of the bulk, which is itself roughly 6.7°C higher than the initial temperature at this stage of loading (a higher final temperature is reached at the end of loading). The displacement field is shown in (a) and (b) after removal of the rigid body motion. The shear band appears markedly on both components of the displacement. Strains are more sensitive to noise, especially for small element sizes (since the number of pixels contributing to the determination of the displacement decreases). Nevertheless both the transverse and axial strains shown in

(d) and (e) clearly reveal the presence of a shear band. The order of magnitude of the measured strain both inside and outside the band is in good agreement with previously published values on a similar Ni-Ti material.

Conclusion

An innovative experimental technique has been proposed to get round the main difficulties encountered during simultaneous thermal and kinematic full field measurements, especially the synchronisation and association steps. This protocol is based on a Digital Image Correlation principle, with a generalized form of the brightness conservation. It uses a sole IR camera and a speckle of emissivity applied on the specimen. A special—yet not restrictive—experimental set-up ensures that the IR images contain only the information relative to the evolution of the specimen temperature, and not the surrounding one.

The evolution of the grey level of the speckle with the local temperature has been experimentally assessed. It has been shown that a very good approximation of this evolution is obtained with a sole parameter thanks to a relevant expression of the evolution. This relationship is then used to extend the brightness conservation law. The displacement and temperature fields are decomposed onto a basis of continuous functions as proposed in finite element methods. An efficient iterative algorithm is developed to jointly determine the kinematic and thermal fields over a whole IR movie.

Though slightly higher, the kinematical measurement uncertainties of this method turn out to be of the same order of magnitude as a usual DIC software. In the case of homogeneous displacement fields, the kinematic standard uncertainty is about 0.025 pixel for a mesh size as small as 12×12 pixels. The thermal standard uncertainty due to the IRIC numerical algorithm is about 10^{-4} °C regardless of the mesh size, i.e., less than the Noise Equivalent to Thermal Difference of the used high-end IR camera. When applied to a NiTi Shape Memory Alloy under tension, this method allows for the measurement of both the thermal and kinematic features of the martensitic transformation bands.

The IRIC is thus a powerful, non intrusive, full field measurement technique. It is a handy solution for coupled measurement since it has the advantage of providing displacement and thermal fields over the exact same time and space discretization with a noticeable accuracy, similar to usual DIC. Of course some improvements can still be made. As an example, the weak spatial resolution of the images provided by IR cameras could be compensated by the high acquisition rate available by using an adequate spatio-temporal correlation. Still, infrared Image Correlation already is a relevant observation and measurement technique for all kind of localised phenomena involving a strong thermomechanical coupling such as phase transformations, crack propagation, shear band formation, and fatigue damage.

References

1. Chasiotis I, Knauss WG (2002) A new microtensile tester for the study of mems materials with the aid of atomic force microscopy. *Exp Mech* 42(1):51–57
2. Hild F, Roux S, Gras R, Guerrero N, Marante ME, Florez-Lopez J (2009) Displacement measurement technique for beam kinematics. *Opt Lasers Eng* 47(3–4):495–503
3. Chrysochoos A, Berthel B, Latourte F, Galtier G, Pagano S, Wattrisse B (2008) Local energy analysis of high-cycle fatigue using digital image correlation and infrared thermography. *J Strain Anal Eng Des* 43:411–421
4. Pottier T, Moutrille MP, Le Cam J-B, Balandraud X, Grédiac M (2009) Study on the use of motion compensation techniques to determine heat sources. Application to large deformations on cracked rubber specimens. *Exp Mech* 49:561–574
5. Schlosser P (2009) Influence of the thermal and mechanical aspects and of their coupling on the homogeneous or localized behavior of NiTi alloys. PhD Thesis, University Joseph Fourier Grenoble
6. Pieczyska EA, Gadaj SP, Nowacki WK, Tobushi H (2006) Phase-transformation fronts evolution for strain- and stress-controlled tension tests in TiNi shape memory alloy. *Exp Mech* 46:531–542
7. Orteu JJ, Rotrou Y, Sentenac T, Robert L (2008) An innovative method for 3-D shape, strain and temperature full-field measurement using a single type of camera: principle and preliminary results. *Exp Mech* 48:163–179
8. Favier D, Louche H, Schlosser P, Orgéas L, Vacher P, Debove L (2007) Homogeneous and heterogeneous deformation mechanisms in an austenitic polycrystalline Ti-50.8 at. % Ni Thin tube under tension. Investigation via temperature and strain fields measurements. *Acta Mater* 55:5310–5322
9. Bodelot L, Sabatier L, Charkaluk E, Dufrénoy P (2009) Experimental setup for fully coupled kinematic and thermal measurements at the microstructure scale of an AISI 316L steel. *Mater Sci Eng A* 501:52–60
10. Gaussorgues G (1994) Infrared thermography. Microwave Technology Series 5. Chapman & Hall Ed., London, 508 pp.
11. Besnard G, Hild F, Roux S (2006) “Finite-element” displacement fields analysis from digital images: application to Portevin–Le Côtelier bands. *Exp Mech* 46:789–803
12. Sun QP, Zhong Z (2000) An inclusion theory for the propagation of martensite band in NiTi shape memory alloy wires under tension. *Int J Plast* 16:1169–1187
13. Sittner P, Liu Y, Novak V (2005) On the origin of Lüders-like deformation of NiTi shape memory alloys. *J Mech Phys Solids* 53:1719–1746
14. Daly S, Ravichandran G, Bhattacharya K (2007) Stress-induced martensitic phase transformation in thin sheets of Nitinol. *Acta Mater* 55:3593–3600
15. Sun QP, Li ZQ (2002) Phase transformation in superelastic NiTi polycrystalline micro-tubes under tension and torsion from localization to homogeneous deformation. *Int J Solids Struct* 39:3797–3809
16. Feng P, Sun QP (2006) Experimental investigation on macroscopic domain formation and evolution in polycrystalline NiTi microtubing under mechanical force. *J Mech Phys Solids* 54:1568–1603
17. Schlosser P, Louche H, Favier D, Orgéas L (2007) Thermomechanical observations of phase transformations during tensile Tests of NiTi tubes. *Strain* 43:260–271
18. Gadaj SP, Nowacki WK, Pieczyska EA (2002) Temperature evolution in deformed shape memory alloy. *Infrared Phys Technol* 43:151–155
19. Lavernhe-Taillard K, Maynadier A, Poncelet M, Benallal A (2009) Caractérisation thermo-mécanique et modélisation des bandes de transformation dans un Alliage à Mémoire de Forme. In: *Proceeding of 19ème Congrès Français de Mécanique*, Marseille, France
20. Schulz M, Caldwell L (1995) Nonuniformity correction and correctability of infrared focal plane arrays. *Infrared Phys Technol* (4):763–777